PAPER • OPEN ACCESS

The transport of low-frequency turbulence in the super-Alfvénic solar wind

To cite this article: L Adhikari *et al* 2015 *J. Phys.: Conf. Ser.* **642** 012001

View the article online for updates and enhancements.

The transport of low-frequency turbulence in the super-Alfvénic solar wind

L Adhikari[1,2], G P Zank[1,2], R Bruno[3], D Telloni[4], P Hunana[2], A Dosch[2], R Marino[5], and Q Hu[1,2]

[1]Department of Space Science, University of Alabama in Huntsville, Huntsville, AL 35899, USA

[2]Center for Space Plasma and Aeronomic Research (CSPAR), University of Alabama in Huntsville, Huntsville,
AL 35899, USA

[3] (INAF-IAPS Istituto di Astrofisica e Planetologia Spaziali, Via del Fosso del Cavaliere 100, I-00133 Roma, Italy

[4] INAF-Astrophysical Observatory of Torino, Via Osservatorio 20, I-10025 Pino Torinese, Italy

[5] National Center for Atmospheric Research, P.O. Box 3000, Boulder, CO 80307, USA

E-mail: la0004@uah.edu

Abstract. Understanding the transport of low-frequency turbulence in an expanding magnetized flow is very important in analyzing numerous problems in space physics and astrophysics. Zank et al 2012 developed six general coupled turbulence transport equations, including the Alfvén velocity to describe the transport of low-frequency turbulence for any inhomogeneous flows, including sub-Alfvénic coronal flows, and super-Alfvénic solar wind flows. Here, we solve the 1D steady state six coupled turbulence transport equations of Zank et al. 2012, and the transport equation corresponding to the solar wind temperature in the super-Alfvénic solar wind flows from 0.29 to 100 AU without the Alfvén velocity. We calculate turbulent quantities corresponding to $Voyager$ 2 data sets for three cases; i) a positive and negative sign of B_r; ii) the azimuthal angle $\phi = \tan^{-1}(B_t/B_r)$, and iii) a positive and negative sign of B_t, where B_r and B_t are the radial and transverse components of the interplanetary magnetic field, respectively. We compare our theoretical results to the observational results, and find good agreement between them.

1. Introduction

Turbulence is very common in the astrophysical plasma such as the solar corona, the solar wind, the interstellar medium and so on. Turbulence is created in situ by the presence of gradients in density, pressure, velocity, vorticity, temperature, magnetic fields, and current density. For example, gradients in velocity occur at interfaces between high and low speed solar wind flows. Similarly, gradients in density, pressure, velocity and magnetic field are intrinsic properties of a shock. The solar wind may therefore be considered as a huge laboratory for studying turbulence ([1–3]), and has been studied from the beginning of the space age ([1–7]). The realization that the Reynolds number of the solar wind is very large (of the order of $R_e \sim 10^8$ [8]) also supports the notion that the solar wind is highly turbulent.

Numerous problems in space science and astrophysics require a detailed understanding of the transport and dissipation of low-frequency turbulence in an expanding magnetized flow. The

development of turbulence transport model equations started with the first observed fluctuations in the interplanetary medium. Paul J. Coleman studied the spectral properties of plasma fluctuations in the solar wind using Mariner 2 spacecraft magnetometer data [5], and found that the spectra of magnetic fluctuations was similar to that of velocity fluctuations, as predicted by Kriachnan 1965 [9]. On the other hand, [10] and [4] studied the Mariner 5 magnetometer and plasma data set using wave analysis, and found that the radial component of the interplanetary magnetic field (IMF) and the solar wind are highly correlated. Based on observational studies, [10] and [4] introduced the idea that solar wind fluctuations may be regarded as a superposition of non-interacting MHD waves, specifically Alfvén waves. The Alfvénic fluctuations do not damp as rapidly as slow and fast modes MHD waves, and hence Alfvén waves dominate fluctuations observed in the heliosphere.

One of the most interesting characteristics of the solar wind is the observed radial solar wind temperature profile which does not follow the adiabatic cooling profile i.e., $r^{-4/3}$, where r is the heliocentric distance ([11, 12, 13, 14, 15, 16]). The dissipation of turbulence generated in situ is thought to be responsible for heating the solar wind in the inner and outer heliosphere.

Observations show that there exist both inward/backward and outward/forward fluctuations in the solar wind. These oppositely directed propagating modes interact non-linearly such that large scales energy eventually accumulates at small scales, which is eventually dissipated into heat energy. The quantity that defines the energy difference between forward and backward propagating modes is known as the cross helicity. The cross helicity gives us an idea about the characteristics of Alfvén wave propagation. Another important quantity is the residual energy, which measures whether the fluctuating energy resides within the magnetic field or velocity field ([21, 22]). The residual energy is defined as the energy difference between the fluctuating kinetic and magnetic energy. The residual energy is found theoretically and observationally to be negative in the inner and outer heliosphere ([21, 22, 23, 24, 25]), indicating the dominance of fluctuating magnetic energy in the MHD fluctuations.

2. Turbulence transport equations

Since the earliest observations of turbulence in the solar wind, there has been considerable interest in understanding how turbulence is transported. Turbulence transport equations describe the evolution of fluctuations throughout the solar wind and the heliosphere. The traditional approach for modeling the transport of fluctuations was based on the Wentzel-Kramers-Brillouin (WKB) theory ([26, 37, 28]), which is a linearized wave description. The WKB model considers non-interacting propagating waves, and therefore neglects possible mixing or coupling between propagating modes. However, forward and backward propagating modes can typically be coupled via a three wave interaction mediated by a zero frequency mode. Therefore, several models were developed to address the limitations of the WKB model ([29–32]).

For studying turbulence, the use of the sum and difference of the velocity and magnetic fluctuations, $\mathbf{u}$ and $\mathbf{b}$, respectively, is more convenient to use rather than considering each separately. This is because the incompressible MHD equations can be expressed compactly in terms of the Elsässer variables. The sum and difference of the fluctuations form the Elsässer variables, $\mathbf{z}^{\pm} = \mathbf{u} \pm \mathbf{b}/\sqrt{\mu_0 \rho}$ ([33]), where the fluctuating magnetic field is normalized to the Alfvén unit and ρ is the solar wind density. The parameters $\mathbf{z}^{\pm}$ describe two oppositely propagating modes, and their directions are defined with respect to the large-scale magnetic field $\mathbf{B}_0$.

WKB theory assumes that interplanetary fluctuations are Alfvén waves, from which it follows that the variance in the fluctuating magnetic field $\langle b^2 \rangle$ decays as r^{-3}, where r is the heliocentric distance. WKB theory successfully explains the radial evolution of magnetic fluctuations within ~ 8 AU. However, beyond 8 AU, WKB theory fails to explain the observed evolution of the variance in magnetic field fluctuations. The reason is that WKB theory is a linear theory for

small amplitude Alfvén waves propagating in the inhomogeneous solar wind. Zank et al 1996 [34] developed two coupled turbulence transport equations, which describe the transport of the fluctuating magnetic energy density E_b $(= \langle b^2 \rangle / \mu_0 \rho)$ and the correlation length λ beyond ~ 1 AU. However, [34] cannot be applied within 1 AU because it assumes zero cross helicity and constant Alfvén ratio. Later, [35], [36], and [37] further developed the turbulence transport models using the similar formalism of [34]. These models can be applied within 1 AU, but they do not include the Alfvén velocity and also cannot describe the residual energy. The Alfvén velocity is very important in sub-Alfvénic coronal flows. Similarly, the residual energy is an important quantity for the MHD fluctuations. To address all these limitations, Zank et al 2012 [38] developed six coupled turbulence transport equations that describe the transport of energy in forward and backward propagating modes, the residual energy, the correlation length corresponding to forward and backward propagating modes, and the correlation length for the residual energy. Since [38] includes the Alfvén velocity, we can use the transport equations to study turbulence in sub-Alfvénic coronal flows as well as study turbulence in the super-Alfvénic solar wind. In the latter case, we neglect the Alfvén velocity in the turbulence transport equations.

The 1D steady-state six coupled turbulence transport equations of [38] in terms of $f = \langle z^{+2} \rangle$ and $g = \langle z^{-2} \rangle$ and $a = 1/2$ and $b = 0$ and neglecting the Alfvén velocity, in a spherical coordinate system are given by

$$U\frac{df}{dr} + U\frac{f}{r} + U\frac{E_D}{r} - \Gamma E_D = -2\frac{fg^{1/2}}{\lambda^+} + 2\left\langle \mathbf{S}^+ \cdot \mathbf{z}^+ \right\rangle; \tag{1}$$

$$U\frac{dg}{dr} + U\frac{g}{r} + U\frac{E_D}{r} - \Gamma E_D = -2\frac{gf^{1/2}}{\lambda^-} + 2\left\langle \mathbf{S}^- \cdot \mathbf{z}^- \right\rangle; \tag{2}$$

$$U\frac{dE_D}{dr} + U\frac{E_D}{r} + \left(\frac{U}{r} - \Gamma\right)\frac{f+g}{2} = -E_D\left[\frac{f^{1/2}}{\lambda^-} + \frac{g^{1/2}}{\lambda^+}\right] + \left\langle \mathbf{S}^- \cdot \mathbf{z}^+ \right\rangle + \left\langle \mathbf{S}^+ \cdot \mathbf{z}^- \right\rangle; \tag{3}$$

$$U\frac{d\lambda^+}{dr} + \frac{E_D}{f}\left[\frac{U}{2r} - \frac{\Gamma}{2}\right](\lambda_D - 2\lambda^+) = 2g^{1/2} - 2\frac{\langle \mathbf{z}^+ \cdot \mathbf{S}^+ \rangle}{f}\lambda^+; \tag{4}$$

$$U\frac{d\lambda^-}{dr} + \frac{E_D}{g}\left[\frac{U}{2r} - \frac{\Gamma}{2}\right](\lambda_D - 2\lambda^-) = 2f^{1/2} - 2\frac{\langle \mathbf{z}^- \cdot \mathbf{S}^- \rangle}{g}\lambda^-; \tag{5}$$

$$U\frac{d\lambda_D}{dr} + \left(\frac{U}{r} - \Gamma\right)\frac{f+g}{E_D}\left(\frac{f\lambda^+ + g\lambda^-}{f+g} - \frac{\lambda_D}{2}\right) = \lambda_D\left[\frac{f^{1/2}}{\lambda^-} + \frac{g^{1/2}}{\lambda^+}\right] - \frac{\lambda_D}{E_D}\left[\left\langle \mathbf{z}^- \cdot \mathbf{S}^+ \right\rangle \right. $$
$$\left. + \left\langle \mathbf{z}^+ \cdot \mathbf{S}^- \right\rangle\right], \tag{6}$$

where f is the energy corresponding to backward propagating modes, g is the energy corresponding to forward propagating modes, $E_D = \left\langle u^2 \right\rangle - \left\langle b^2/\mu_0\rho \right\rangle$ is the residual energy, λ^+ is the correlation length corresponding to backward propagating modes, λ^- the correlation length corresponding to forward propagating modes, and λ_D the correlation length corresponding to the residual energy. Terms such as $\left\langle \mathbf{S}^\pm \cdot \mathbf{z}^\pm \right\rangle$ refer to sources of turbulence, which we discuss later. The parameter $\Gamma(= n_i n_j \partial U_j / \partial U_i)$ is the shear mixing term, which we neglect by choosing $\Gamma = 0$.

In Equations (1), (2), and (3), the first terms on the right hand side indicate the dissipation for the energy in backward and forward propagating modes and the residual energy. By combining

all three dissipation terms, we can write the evolution equation for the solar wind temperature as [18-21, 25]

$$U\frac{dT}{dr} + (\gamma - 1)\frac{2UT}{r} = \frac{1}{9}\frac{m_p}{k_B}\alpha\left[\frac{fg^{1/2}}{\lambda^+} + \frac{gf^{1/2}}{\lambda^-} + E_D\left(\frac{f^{1/2}}{\lambda^-} + \frac{g^{1/2}}{\lambda^+}\right)\right],\tag{7}$$

where $\gamma = 5/3$ is the adiabatic index, m_p is the proton mass, k_B is the Boltzmann constant, and α is the von Kármán-Taylor constant. We choose $\alpha = 1$ ([18]). The first term inside the square bracket in Equation (7) corresponds to the dissipation term for the energy in backward propagating modes, the second term to the dissipation term for energy in forward propagating modes, and the third term is the dissipation term for the residual energy.

The total turbulent energy E_T, the cross helicity E_C, the fluctuating magnetic energy density E_b, and the Alfvén ratio r_A can be expressed in terms of f and g as ([38])

$$E_T = \left\langle u^2 \right\rangle + \left\langle b^2/\mu_0\rho \right\rangle = \frac{f+g}{2};\tag{8}$$

$$E_C = 2\left\langle \mathbf{u}\cdot\mathbf{b}/\sqrt{\mu_0\rho} \right\rangle = \frac{g-f}{2};\tag{9}$$

$$E_b = \left\langle \frac{b^2}{\mu_0\rho} \right\rangle = \frac{E_T - E_D}{2} = \frac{f+g-2E_D}{4};\tag{10}$$

$$r_A = \frac{\left\langle u^2 \right\rangle}{\left\langle b^2/\mu_0\rho \right\rangle} = \frac{E_T + E_D}{E_T - E_D} = \frac{f+g+2E_D}{f+g-2E_D};\tag{11}$$

$$\left\langle u^2 \right\rangle = \frac{E_T + E_D}{2} = \frac{f+g+2E_D}{2}.\tag{12}$$

These turbulent quantities have been previously studied by several authors. However, here we apply a more sophisticated set of turbulence transport model equations to calculate these quantities, and then we compare to *Voyager* 2 observations.

3. Sources of turbulence

There are in principle three types of turbulence sources, stream shear ([5]), shock waves ([39]), and pickup ions ([40]). The first two sources are important within $4-5$ AU, and the third source is important beyond the ionization cavity ($\gtrsim 6-10$ AU). The shear source can be written in a form similar to that of [34] and [25],

$$\left\langle \mathbf{S}^+\cdot\mathbf{z}^+ \right\rangle = C_{\mathrm{sh}}(f)\frac{\Delta U_{\mathrm{shear}}}{r}f;\tag{13}$$

$$\left\langle \mathbf{S}^-\cdot\mathbf{z}^- \right\rangle = C_{\mathrm{sh}}(g)\frac{\Delta U_{\mathrm{shear}}}{r}g;\tag{14}$$

$$\left\langle \mathbf{S}^-\cdot\mathbf{z}^+ \right\rangle + \left\langle \mathbf{S}^+\cdot\mathbf{z}^- \right\rangle = [C_{\mathrm{sh}}(f) + C_{\mathrm{sh}}(g)]\frac{\Delta U_{\mathrm{shear}}}{r}E_D,\tag{15}$$

where $C_{\mathrm{sh}}(f)$ and $C_{\mathrm{sh}}(g)$ are the strengths of shear interaction corresponding to backward and forward propagating modes, respectively, and $\Delta U_{\mathrm{shear}}$ ($= 350$ kms^{-1}) is the velocity difference between the fast and slow solar wind speed. It is assumed that shear driving generally supplies energy to the forward and backward propagating modes at an equal rate i.e., $C_{sh}(f) = C_{sh}(g)$. Similarly, the stream source of turbulence due to shocks for backward and forward propagating modes, and residual energy respectively is given by

$$\left\langle \mathbf{S}^+\cdot\mathbf{z}^+ \right\rangle = C_{\mathrm{shock}}(f)\frac{\Delta U_{\mathrm{shock}}}{r}f;\tag{16}$$

$$\left\langle \, \mathbf{S}^- \cdot \mathbf{z}^- \, \right\rangle = C_{\text{shock}}(g) \frac{\Delta U_{\text{shock}}}{r} g; \tag{17}$$

$$\left\langle \, \mathbf{S}^- \cdot \mathbf{z}^+ \, \right\rangle + \left\langle \, \mathbf{S}^+ \cdot \mathbf{z}^- \, \right\rangle = [C_{\text{shock}}(f) + C_{\text{shock}}(g)] \frac{\Delta U_{\text{shock}}}{r} E_D, \tag{18}$$

where $C_{\text{shock}}(f)$ and $C_{\text{shock}}(g)$ parametrize the generation of energy for the backward and forward propagating modes, respectively, and ΔU_{shock} is the difference between the upstream and downstream speed of the shock. Finally, the pickup ion source of turbulence for backward and forward propagating modes, and the residual energy is

$$\left\langle \, \mathbf{S}^+ \cdot \mathbf{z}^+ \, \right\rangle = \frac{1}{2} \frac{f_D(f) n_H^\infty U V_A}{n_{\text{sw}} \tau_{\text{ion}}} \exp\left[-\frac{\lambda \chi}{r \sin \chi} \right]; \tag{19}$$

$$\left\langle \, \mathbf{S}^- \cdot \mathbf{z}^- \, \right\rangle = \frac{1}{2} \frac{f_D(g) n_H^\infty U V_A}{n_{\text{sw}} \tau_{\text{ion}}} \exp\left[-\frac{\lambda \chi}{r \sin \chi} \right]; \tag{20}$$

$$\left\langle \, \mathbf{S}^- \cdot \mathbf{z}^+ \, \right\rangle + \left\langle \, \mathbf{S}^+ \cdot \mathbf{z}^- \, \right\rangle = 0. \tag{21}$$

Here, $0 < f_D(f) < 1$ and $0 < f_D(g) < 1$, and are functions of V_A/U which determines the fraction of pickup ion energy transferred into excited waves. It is assumed that pickup ions provide energy equally to forward and backward propagating modes i.e., $f_D(f) \sim f_D(g)$. The parameter n_H^∞ is the number density of interstellar neutrals, τ_{ion}^0 is the neutral ionization time at 1 AU, λ is the ionization cavity length scale, and χ is the angle between the observation point and the upstream direction.

4. Results

We solve the seven coupled equations (1)–(7) numerically using a Runge-Kutta 4th order method from 0.29 to 100 AU, and compare the theoretical results to $Voyager$ 2 observations. The initial conditions for the solar wind parameters at 0.29 AU are, $f = 753$ (kms^{-1})^2, $g = 13,515$ (kms^{-1})^2, $E_D = -57.07$ (kms^{-1})^2, $\lambda^+ = 0.00143$ AU, $\lambda^- = 0.000779$ AU, $\lambda_D = 0.0204$ AU, and $T = 3.5 \times 10^5$ K. For the observations, we use $Voyager$ 2 1 hour resolution data sets from 1977 though 2005 to calculate the solar wind parameters from 1 to ~ 75 AU. The process to find the observed values is as follows; we consider R, T, and N components of the magnetic and velocity fields, the solar wind density, and the solar wind temperature. At first, the sequential 10 hours interval data sets are considered, and then the mean field corresponding to the magnetic field, the solar wind speed, the solar wind temperature, and the solar wind density is calculated. After that the fluctuating magnetic field $\mathbf{b}$ and solar wind speed $\mathbf{u}$ are calculated for each 10 hour interval. Elsässer variables are then calculated by using $\mathbf{z}^\pm = \mathbf{u} \pm \mathbf{b}/\sqrt{\mu_0 \rho}$, where μ_0 is a permeability of free space, and ρ is the mean solar wind density. Note that Elsässer variables as well as the turbulent quantities are calculated for three cases; i) positive and negative sign of the radial component of the magnetic field B_r; ii) $0° < \phi < 180°$ and $180° < \phi < 360°$, where $\phi = \tan^{-1}(B_t/B_r)$ is an azimuthal angle, and iii) positive and negative sign of the T component of the magnetic field B_t. Here, $0° < \phi < 180°$ identifies one polarity of the magnetic field, and $180° < \phi < 360°$ the other polarity ([41-43]). In our case, we assume that $0° < \phi < 180°$ represents outwardly directed magnetic field, and $180° < \phi < 360°$ inwardly directed magnetic field.

We use two criteria, i) the mean square fluctuations of the velocity and magnetic field should be smaller than the square of mean fields and ii) each interval should contain at least five good data points, in each 10 hour interval data set. The turbulent quantities such as the Elsässer variables, the residual energy, the solar wind density, the solar wind temperature, the variance in the magnetic field fluctuations and the fluctuating kinetic energy, are calculated only if the criteria ii) is satisfied, otherwise we neglect the interval and move then to next interval. We

follow similar procedure until the end of each yearly data sets. We use criteria i) to remove irregular fluctuations from each interval. From the observed Elsässer variables, the variances are calculated. These variances correspond to the energy in forward and backward propagating modes. We then use Equations (8)–(12) to find other turbulent quantities. Note that we calculate the R, T, and N components as well as the total turbulent quantities as a function of heliocentric distance. Finally, we smooth the observed values by taking 50 10-hours interval data sets from an intermediate file, where we use criteria i). The remaining observed quantities are averaged to find the smoothed observed values.

To find the correlation length corresponding to forward and backward propagating modes and the residual energy, 20 hour interval data sets are considered. Elsässer variables are then calculated in each 20 hour interval data sets, which are then used to calculate the auto-correlation and cross-correlation function. The auto-correlation function is used to find the correlation length for the forward and backward propagating modes, and the cross-correlation function for the correlation length corresponding to the residual energy ([25,44]). The correlation length corresponds to lag r where the auto- or cross-correlation function becomes 1/e of the maximum value.

Figure 1 shows the comparison between the theoretical and observed correlation length corresponding to different energy modes. The blue curve denotes the correlation length for forward propagating modes, the red curve for backward propagating modes, and the green curve for the residual energy. Similarly, the scatter circles, triangles, and diamonds symbol identify
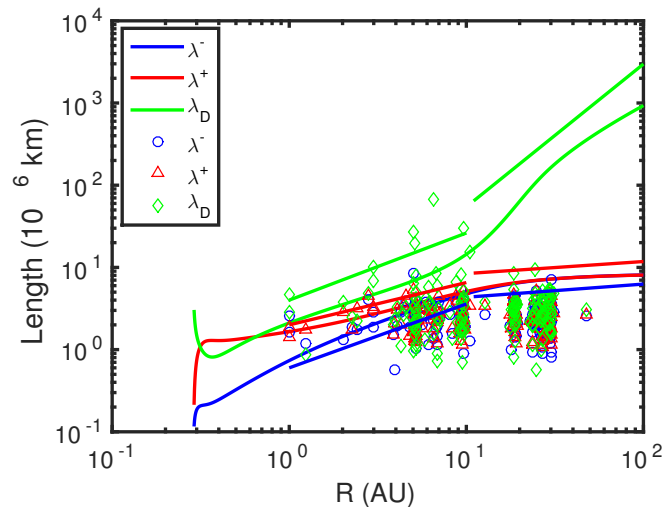

Figure 1. Comparison between the theoretical and observed correlation lengths corresponding to forward and backward propagating modes and the residual energy as functions of heliocentric distance. The solid blue, red and green straight lines guide the theoretical correlation lengths between 1–10 AU and beyond 10 AU (see text for details).

the observed correlation length for forward and backward propagating modes, and the residual energy, respectively. The two correlation lengths (blue and red curves) approach one another beyond ~ 1 AU, and then become approximately equal beyond $\sim 20-30$ AU. On the other hand, the correlation length for the residual energy (green curve) increases beyond 10 AU. The increase in the residual correlation length is due to the assumption that we set the pickup ion source for the residual energy to zero. We believe that pickup ions in the outer heliosphere beyond the ionization cavity generate Alfvénic fluctuations such that there is equipartition between the fluctuating kinetic and magnetic energy. The pickup ion source for the residual energy may need

further investigation.

In Figure 1, the solid blue, red, and green straight lines describe the power law fits to different parts of the blue, red, and green curves, respectively, such that between $1 - 10$ AU (non-PUI influenced), and > 10 AU (PUI mediated). The slopes of the blue, red, and green straight lines between $1 - 10$ AU are 0.7772, 0.515, and 0.8166, respectively, and for > 10 AU are 0.16, 0.14, and 1.737, respectively. In the case of blue and red straight lines, the slopes between 1–10 AU are large so that there are significant increments in the correlation lengths, however, there are no significant increments in the correlation lengths beyond 10 AU since the slopes are small. On the other hand, the slope corresponding to the green curve is larger beyond 10 AU than between 1–10 AU, which indicates that the correlation length for the residual energy should increase faster beyond 10 AU than between 1–10 AU.

4.1. Turbulent quantities related to a positive and negative sign of B_r
As mentioned earlier, we calculate the turbulent quantities corresponding to a positive and a negative sign of B_r, and compare them to our theoretical results. The comparisons between the
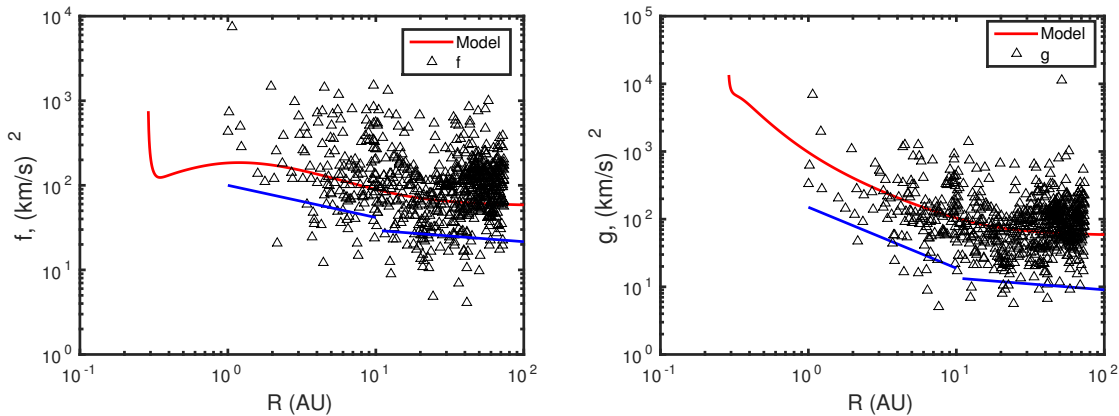

Figure 2. Left: Comparison between the theoretical and observed energy in backward propagating modes as a function of heliocentric distance. Right: Comparison between the theoretical and observed energy in forward propagating modes as a function of heliocentric distance. Solid curves are theoretical results and scatter triangles are total observed values. The solid blue straight lines guide the solid curves between 1-10 AU and beyond 10 AU (see text for details).

theoretical and observed energy in backward and forward propagating modes are shown in the left and right panel of Figure 2, respectively. The left panel of Figure 2 shows that the energy in backward propagating modes decreases sharply at first, increases until $\sim 1 - 2$ AU, and then decreases with increasing heliocentric distance. The comparison between the theoretical and observed f shows that both result follow a similar trend i.e., both decrease gradually as a function of heliocentric distance. The right panel of Figure 2 also shows that both the theoretical and observed g decrease monotonically with increasing heliocentric distance. Furthermore, the left panel of Figure 2 shows an important characteristic in that backward propagating modes are generated within $\sim 1 - 2$ AU. The generation of backward modes is due to the presence of a shear source of turbulence. Furthermore, in the figure, the blue straight lines describe the power law fits to different parts (between 1–10 AU and beyond 10 AU) of the red curves. The slopes of the straight lines between 1–10 AU for f and g are -0.3804 and -0.9012, respectively, and beyond 10 AU are -0.1343 and -0.1725, respectively. The slopes corresponding to different parts of the curves indicate that f and g decrease faster between 1–10 AU than beyond 10 AU.

The left and right panels of Figure 3 illustrate the comparison between the theoretical and observed result for the total turbulent energy E_T and the fluctuating magnetic energy density E_b as a function of heliocentric distance, respectively. To calculate the total turbulent energy and
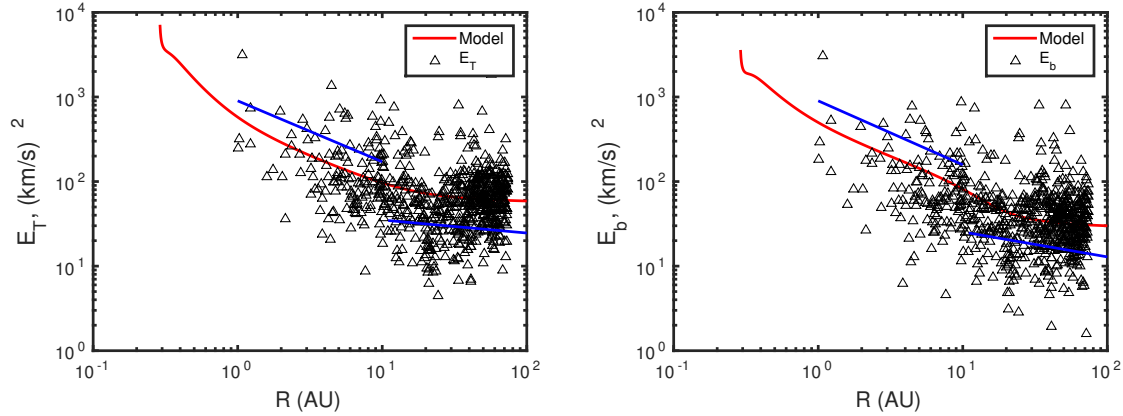

Figure 3. Left: Comparison between the theoretical and observed total turbulent energy as a function of heliocentric distance. Right: Comparison between the theoretical and observed fluctuating magnetic energy density as a function of heliocentric distance. Solid curves are theoretical results and scatter triangles are observational results. The solid blue straight lines guide the solid curves between 1-10 AU and beyond 10 AU (see text for details).

the fluctuating magnetic energy density, we use Equations (8) and (9), respectively. The result shows that the theoretical and observed E_T decrease gradually with increasing heliocentric distance. Similarly, the theoretical and observed E_b decrease monotonically with increasing heliocentric distance. In the left and right plots of Figure 3, the blue straight lines describe the power law fits to different parts of the curves, between 1–10 AU and beyond 10 AU. In the left figure, the slope of the blue line between 1–10 AU is -0.7206 and beyond 10 AU is -0.1538. Similarly, in the right plot, the slopes between 1–10 AU and beyond 10 AU are -0.7565 and -0.2949, respectively. Both E_T and E_b have larger negative slopes between 1–10 AU than beyond 10 AU so that these quantities between 1–10 AU decrease faster in comparison to that of beyond 10 AU.

The left and right panel of Figure 4 illustrate the comparison between the theoretical and observed magnetic field variance $\langle b^2 \rangle$ and fluctuating kinetic energy $\langle u^2 \rangle$ as a function of heliocentric distance, respectively. The left panel of Figure 4 shows good agreement between the theoretical and observed $\langle b^2 \rangle$ from 1 to ~ 75 AU. The right panel of Figure 4 shows that the theoretical $\langle u^2 \rangle$ cannot reproduce the observed $\langle u^2 \rangle$ within ~ 7 AU, however, the theoretical $\langle u^2 \rangle$ is consistent with the observed $\langle u^2 \rangle$ beyond ~ 7 AU. In the left panel of Figure 4, the blue straight lines describe the power law fits to the theoretical results between 1–10 AU and beyond 10 AU. The slopes of the blue lines between 1–10 AU and beyond 10 AU are -2.7565 and -2.2949, respectively. The different slopes indicates that $\langle b^2 \rangle$ decreases with different power law index within 10 AU and beyond 10 AU, such that the decrease in $\langle b^2 \rangle$ is larger within 10 AU than beyond 10 AU.

The left and right panel of Figure 5 illustrate the comparison between the theoretical and observed normalized residual energy and Alfvén ratio as a function of heliocentric distance, respectively. Recall that the residual energy is defined as the difference between the fluctuating kinetic and magnetic energy, and the Alfvén ratio is the ratio between the fluctuating kinetic and magnetic energy. Close to the Sun, the fluctuating kinetic and magnetic energy are
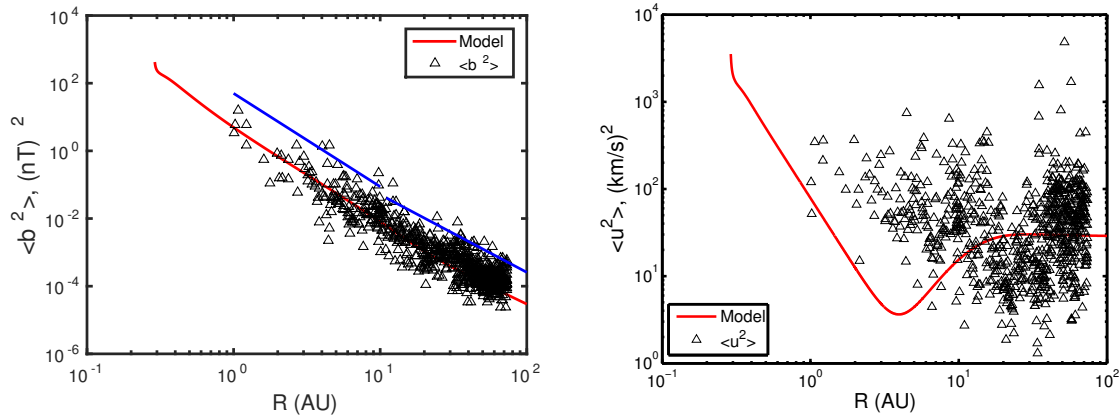
Figure 4. Left: Comparison between the theoretical and observed magnetic field variance as a function of heliocentric distance. Right: Comparison between the theoretical and observed fluctuating kinetic energy as a function of heliocentric distance. Solid curves are theoretical results and scatter triangles are observational results. The solid blue straight lines guide the solid curves between 1-10 AU and beyond 10 AU (see text for details).
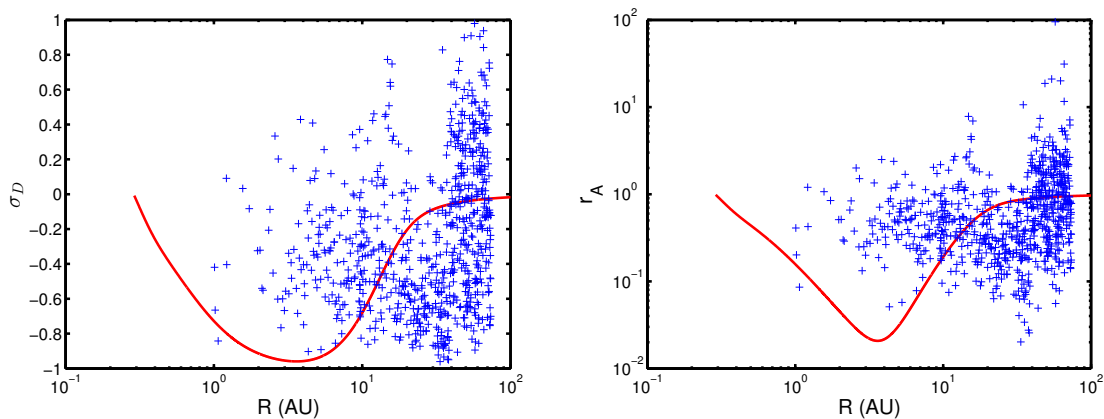

Figure 5. Left: Comparison between the theoretical and observed normalized residual energy as a function of heliocentric distance. Right: Comparison between the theoretical and observed fluctuating Alfvén ratio as a function of heliocentric distance. Solid curves are theoretical results and scatter plus symbols are observational results.

approximately equipartitioned. Therefore, the residual energy is close to 0 at 0.29 AU (left-panel), and the Alfvén ratio close to 1 (right-panel). Both theoretical results for the normalized residual energy and the Alfvén ratio show that the fluctuating magnetic energy in MHD fluctuations increases with increasing heliocentric distance up to $\sim 5-6$ AU, but beyond $\sim 5-6$ AU the fluctuating kinetic energy begins to increase such that the fluctuating kinetic and magnetic energy is approximately equipartitioned beyond $20-30$ AU. The blue plus symbols in the left and right panel of Figure 5 indicate the observed values. There is a large scatter in the observed normalized residual and Alfvén ratio, which may be due to the plasma data.

The left and right panel of Figure 6 illustrate the normalized cross helicity and the solar wind temperature as a function of heliocentric distance, respectively. In the figure, the solid
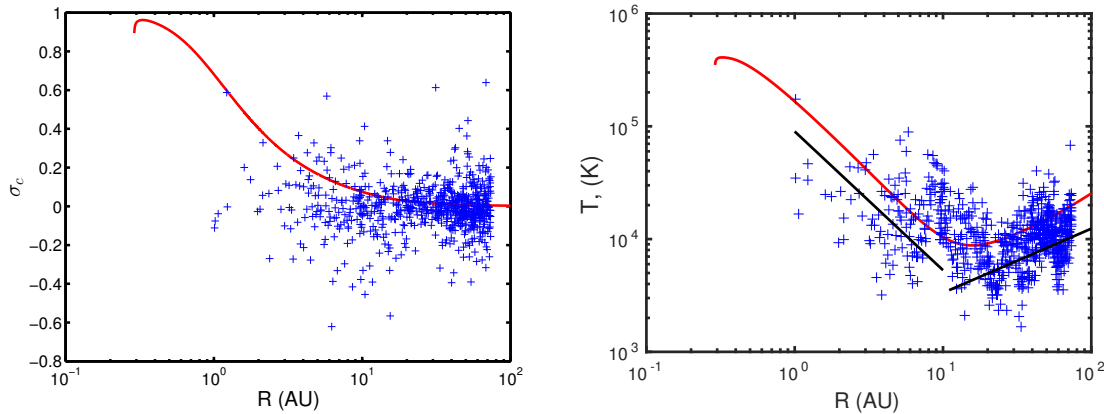
Figure 6. Left: Comparison between the theoretical and observed normalized cross helicity as a function of heliocentric distance. Right: Comparison between the theoretical and observed solar wind temperature as a function of heliocentric distance. Solid curves are theoretical results and scatter plus symbols are observed results. The solid black straight lines guide the solid curves between 1-10 AU and beyond 10 AU (see text for details).

curves are the theoretical results and the scatter plus symbols are the observational results. The left panel shows that the cross helicity decreases gradually with increasing heliocentric distance, and becomes approximately zero beyond ~ 30 AU. The right panel shows that the theoretical and observed solar wind temperature decrease monotonically up to $\sim 10 - 20$ AU, and then increases up to ~ 75 AU. The increase in the temperature beyond $\sim 10 - 20$ AU is due to the presence of pickup ions in the outer heliosphere. In the right panel of Figure 6, the black straight lines describe the power law fits to different parts, between 1–10 AU and beyond 10 AU, of the solar wind temperature (red curve). The slope of the black curve between 1–10 AU is -1.23, and beyond 10 AU is 0.5692, which clearly indicates that the solar wind temperature decreases between 1–10 AU, and increases beyond 10 AU.

4.2. Turbulent quantities related to the azimuthal angle ϕ
The magnetic field in the outer heliosphere is mainly azimuthal, therefore the azimuthal angle ϕ ($=\tan^{-1}(B_t/B_r)$) is used to find the polarity of the magnetic field. The angle ϕ varies between $0°$ and $360°$. Recall that for $0° < \phi < 180°$, the polarity of the magnetic field is outward, and for $180° < \phi < 360°$, the polarity is inward.

The left and right panel of Figure 7 illustrate the energy in backward and forward propagating modes, respectively. The comparison between the theoretical and observed results of f and g shows that both decrease monotonically from ~ 1 AU with increasing heliocentric distance. Moreover, the trends in the observed f and g are similar to the previous observed values obtained by considering the sign of B_r, Figure 2. The left panel of Figure 8 illustrates the total turbulent energy as a function of heliocentric distance, and the right panel the fluctuating magnetic energy density. Figure 8 indicates that the theoretical and observational results of the total turbulent energy and the fluctuating magnetic energy density are in good agreement. These results show that all the energies decay with the expansion of the solar wind.

The left and right panel of Figure 9 describe the variances in the magnetic field and solar wind velocity fluctuations, respectively. The theoretical and observed variance in the fluctuating magnetic field, left panel of Figure 9, show good agreement. On the other hand, the theoretical and observed variance in the fluctuating solar wind velocity, right panel of Figure 9, are consistent
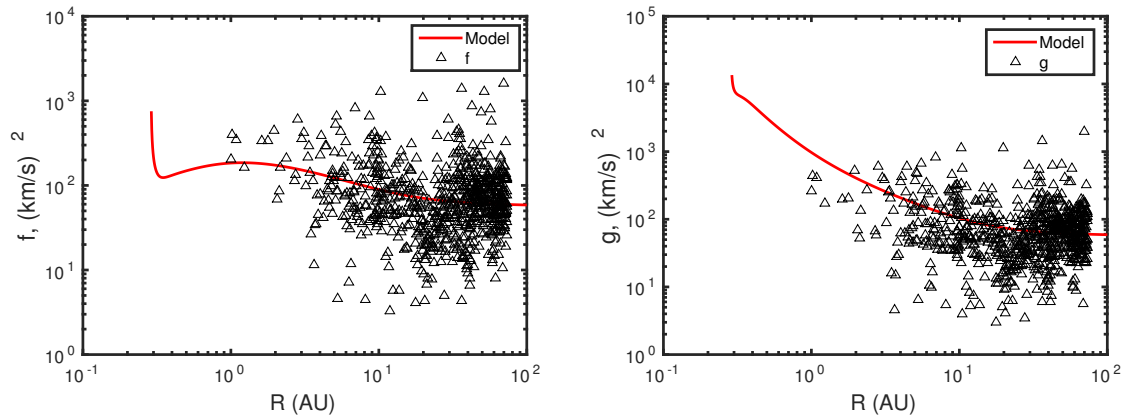
Figure 7. Left: Comparison between the theoretical and observed energy in backward propagating modes as a function of heliocentric distance. Right: Comparison between the theoretical and observed energy in forward propagating modes as a function of heliocentric distance. Solid curves are theoretical results and scatter triangles are observational results.
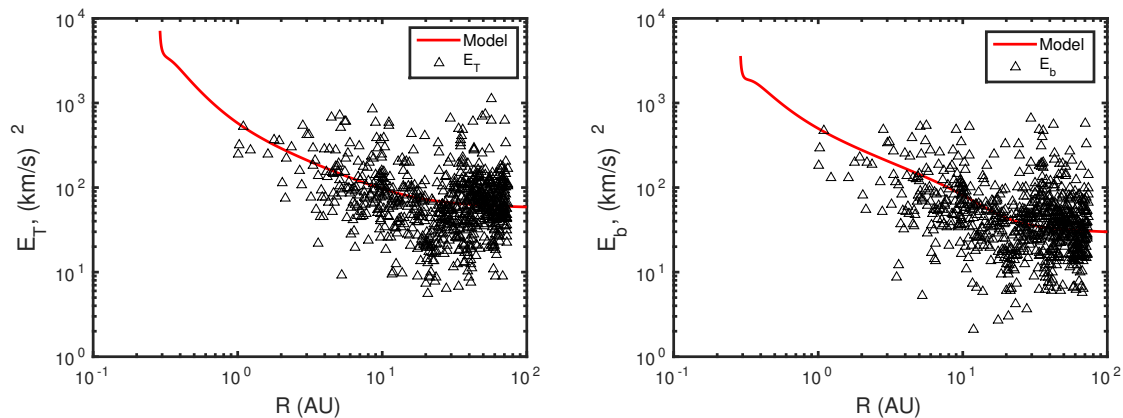

Figure 8. Left: Comparison between the theoretical and observed total turbulent energy as a function of heliocentric distance. Right: Comparison between the theoretical and observed fluctuating magnetic energy density as a function of heliocentric distance. Solid curves are theoretical results and scatter triangles are observational results.

only beyond $\sim 7-8$ AU. The observed values are similar to the previous observed values obtained by considering the sign of B_r, Figure 4.

The left panel of Figure 10 illustrates the normalized residual as a function of heliocentric distance, and the right panel the Alfvén ratio. Similarly, the left and right panel of Figure 11 illustrate normalized cross helicity and the solar wind temperature, respectively. All these observed values are similar to those of the previous observed values as well, Figures 5 and 6.

4.3. Turbulent quantities related to a positive and negative sign of B_t

In this case, we use the sign of B_t to find the polarity of the interplanetary magnetic field. The turbulent quantities are calculated for the positive and negative sign of B_t separately, and then the results are combined.
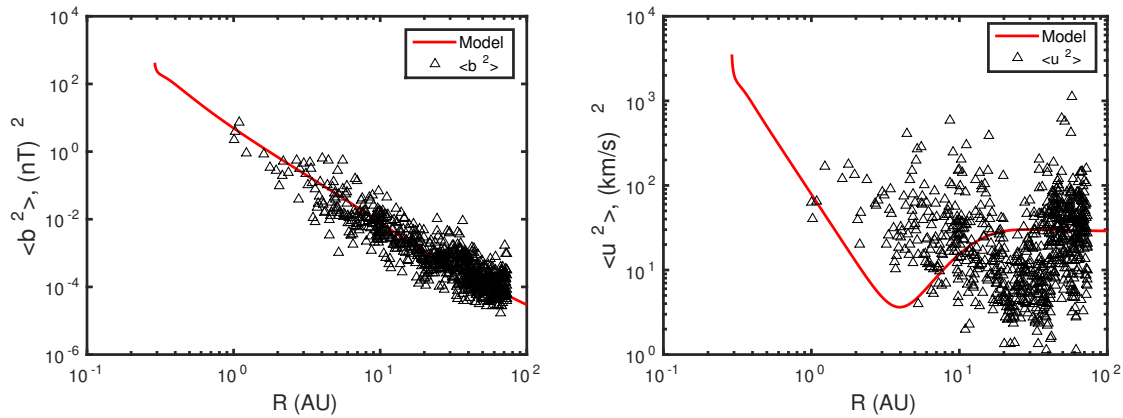
Figure 9. Left: Comparison between the theoretical and observed magnetic field variance as a function of heliocentric distance. Right: Comparison between the theoretical and observed fluctuating kinetic energy as a function of heliocentric distance. Solid curves are theoretical results and scatter triangles are observational results.
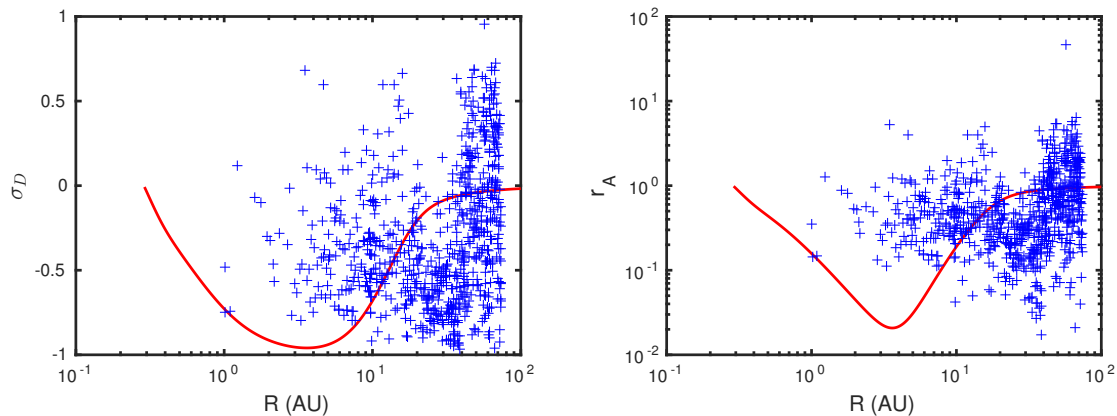

Figure 10. Left: Comparison between the theoretical and observed normalized residual energy as a function of heliocentric distance. Right: Comparison between the theoretical and observed fluctuating Alfvén ratio as a function of heliocentric distance. Solid curves are theoretical results and scatter plus symbols are observational results.

The left and right plots of Figure 12 illustrate the comparison between the theoretical and observed energy in backward and forward propagating modes, respectively. Similarly, the left and right panels of Figure 13 describe the total turbulent energy and the fluctuating magnetic energy density with increasing heliocentric distance, respectively.

The variance in the fluctuating magnetic field and the solar wind velocity as a function of heliocentric distance are shown in the left and right panels of Figure 14, respectively. The normalized residual energy as a function of heliocentric distance is illustrated in Figure 15 (left panel), and the right panel of Figure 15 describes the Alfvén ratio. Furthermore, the normalized cross helicity and the solar wind temperature are shown in the left and right plots of Figure 16. All the comparisons show good agreement between the theoretical and observed results. Moreover, the observed values are also similar to the observed values obtained by considering the azimuthal angle.
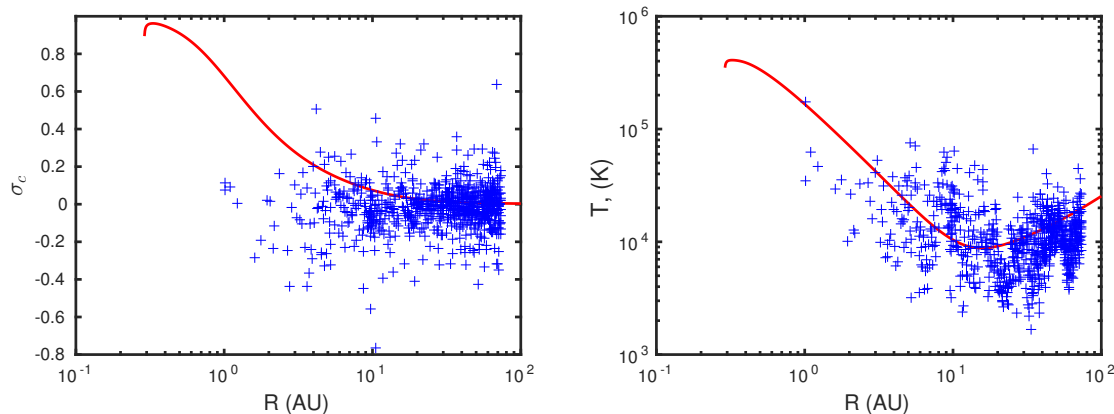
Figure 11. Left: Comparison between the theoretical and observed normalized cross helicity as a function of heliocentric distance. Right: Comparison between the theoretical and observed solar wind temperature as a function of heliocentric distance. Solid curves are theoretical results and scatter plus symbols are observational results.
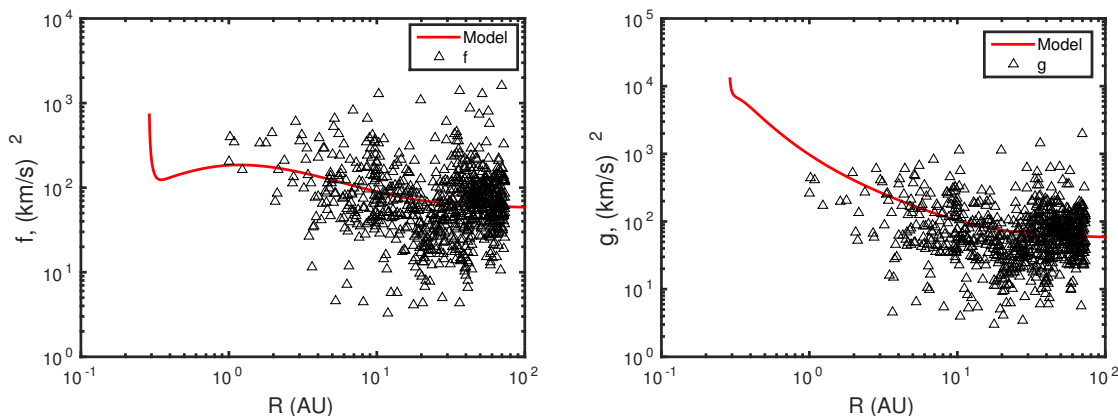

Figure 12. Left: Comparison between the theoretical and observed energy in backward propagating modes as a function of heliocentric distance. Right: Comparison between the theoretical and observed energy in forward propagating modes as a function of heliocentric distance. Solid curves are theoretical results and scatter triangles are observational results.

5. Conclusions

In this paper, we investigated the transport of low-frequency turbulence in the super-Alfvénic solar wind flows theoretically and observationally. We solved the 1D steady state seven coupled turbulence transport equations numerically using a 4th order Runge-Kutta method. We calculated the observed turbulent quantities for three cases; i) a positive and negative sign of B_r, ii) the azimuthal angle ϕ, and iii) a positive and negative sign of B_t. We found that the observed turbulent quantities for the last two cases are the same, and the trends of these observed results are similar to that of the observed results when using the sign of B_r. We found that the theoretical results are consistent with all the observed values. We conclude therefore that the Zank et al 2012 [38] turbulence transport model equations can explain the transport of low-frequency turbulence in the super-Alfvénic solar wind flow.

We considered the evolution of the energy in backward propagating modes from 0.29 to 100
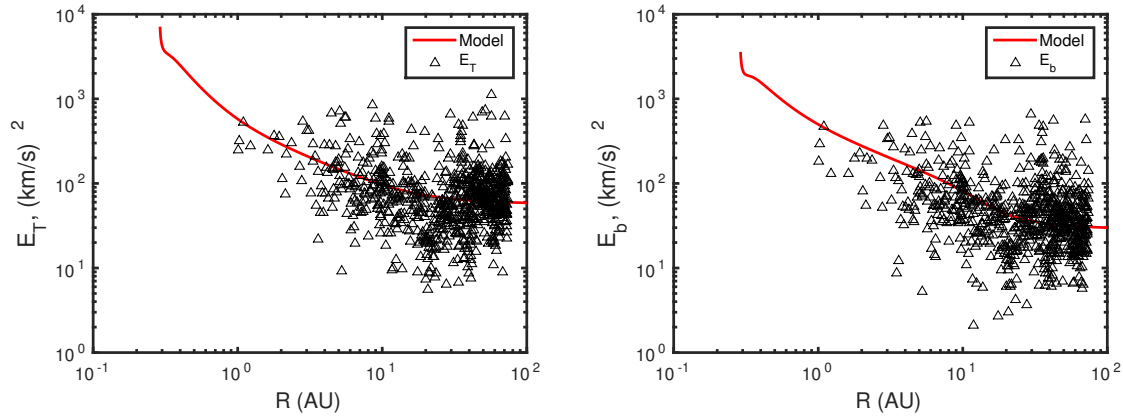
Figure 13. Left: Comparison between the theoretical and observed total turbulent energy as a function of heliocentric distance. Right: Comparison between the theoretical and observed fluctuating magnetic energy density as a function of heliocentric distance. Solid curves are theoretical results and scatter triangles are observational results.
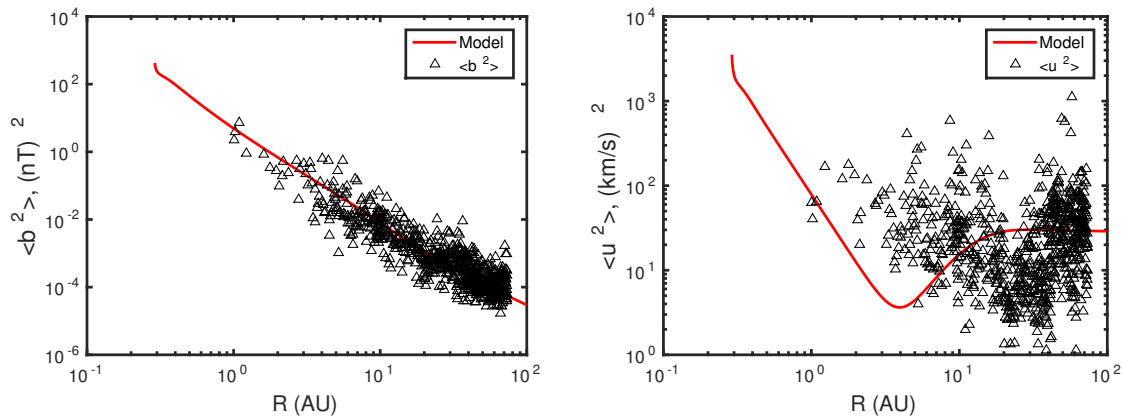

Figure 14. Left: Comparison between the theoretical and observed magnetic field variance as a function of heliocentric distance. Right: Comparison between the theoretical and observed fluctuating kinetic energy as a function of heliocentric distance. Solid curves are theoretical results and scatter triangles are observational results.

AU. Our result shows that backward modes are generated in situ within 1 AU. The creation of backward propagating modes is due to the in situ generation of turbulence by shear driving in the inner heliosphere. We also found that the MHD fluctuations in the solar wind are dominated by the fluctuating magnetic energy between ~ 1 and ~ 10 AU. However, the fluctuating kinetic and magnetic energy is approximately equipartitioned within ~ 1 AU and beyond ~ 10 AU.

We also found that all the energies decay with increasing heliocentric distance at a rate that is slower than would be expected of adiabatic expansion. This is due to the in situ generation of turbulence in the heliosphere. The dissipation of these energies results in plasma heating, which is the reason for the solar wind temperature profile being non-adiabatic. The normalized cross helicity as a function of heliocentric distance is approximately zero beyond ~ 30 AU. It clearly indicates that the energy in forward and backward propagating modes is equipartitioned i.e., $g \sim f$. We find that the correlation lengths corresponding to forward and backward propagating
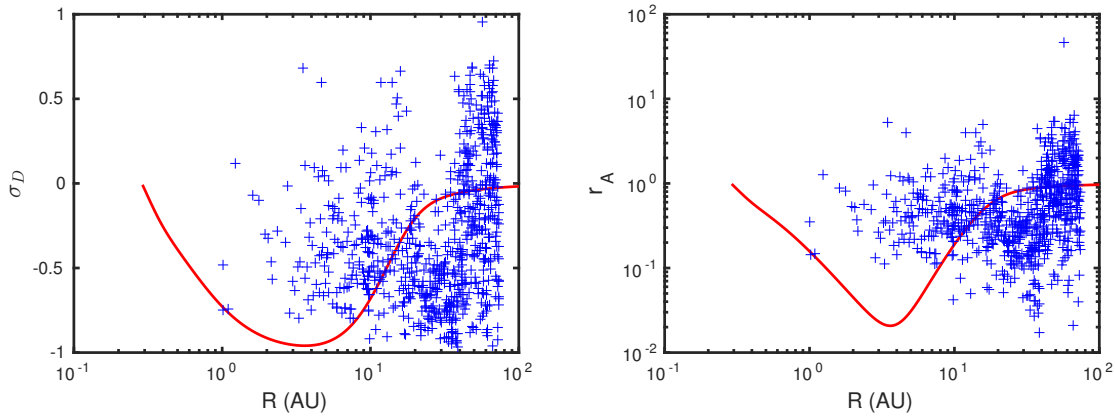
Figure 15. Left: Comparison between the theoretical and observed normalized residual energy as a function of heliocentric distance. Right: Comparison between the theoretical and observed fluctuating Alfvén ratio as a function of heliocentric distance. Solid curves are theoretical results and scatter plus symbols are observational results.
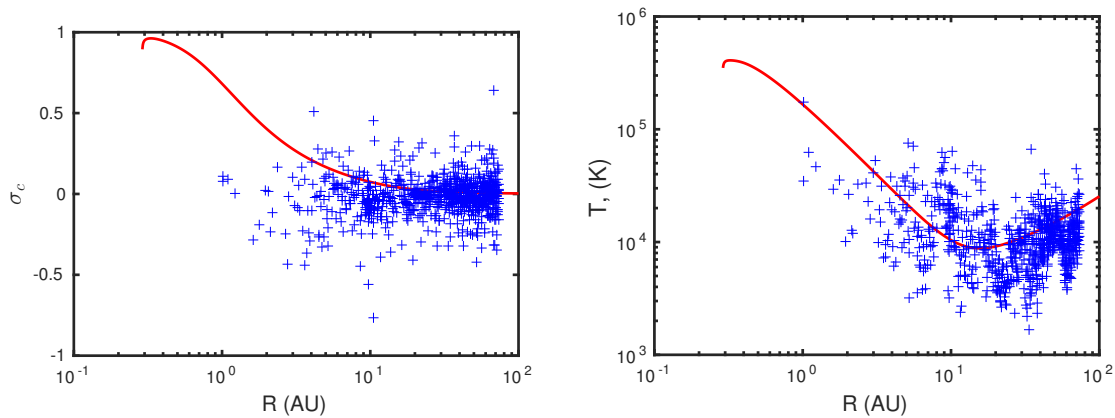

Figure 16. Left: Comparison between the theoretical and observed normalized cross helicity as a function of heliocentric distance. Right: Comparison between the theoretical and observed solar wind temperature as a function of heliocentric distance. Solid curves are theoretical results and scatter plus symbols are observational results.

modes are approximately equal beyond ~ 30 AU i.e., $\lambda^- \sim \lambda^+$. It suggests that if the energy in forward and backward propagating modes is equal, the correlation length corresponding to these energy modes should also be equal, and vice versa. In this situation, the two energy modes dissipate at the same rate.

Appendix A. Comparison to the R, T, and N component turbulent quantities related to a positive and negative sign of B_r

In this section, we compare our theoretical results to the R, T, and N component observed values. The top left plot of Figure 17 illustrates the total turbulent energy as a function of heliocentric distance from 0.29 to 100 AU. The top right plot of Figure 17 illustrate the energy
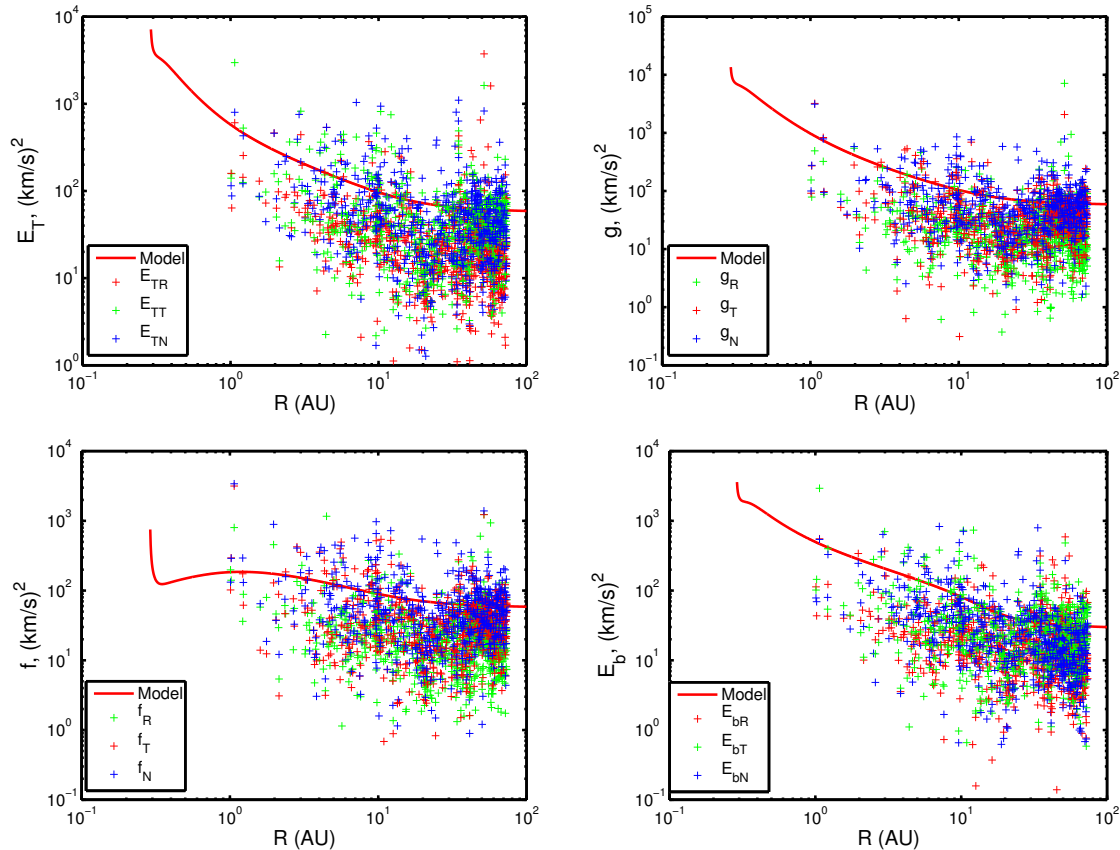

Figure A1. From top left in clockwise order, the plots show respectively the comparison of the theoretical model and the observed total turbulent energy, the energy in forward propagating modes, the fluctuating magnetic energy density, and the energy in backward propagating modes from 0.29 to 100 AU, respectively. The solid curves are theoretical results and the scatter plus symbols are observed values. The suffix R, T, and N indicates the R-component, T-component, and N-component of the observed values.

in forward propagating modes, the bottom left the energy in backward propagating modes, and the bottom right the fluctuating magnetic energy density. In the figure, the red curves denote the theoretical results, and the scatter red, green, and blue plus symbols denote the R, T, and N component observed values. The observed R, T, and N values show that the trend of each component is similar throughout the heliosphere from 1 to ~ 75 AU. These observed values are smaller than the corresponding total observed values, and the trends are similar to the theoretical results as well as to the total observed values.

The left and right panels of Figure 18 illustrate the variance in the fluctuations of the magnetic field and the solar wind speed with increasing heliocentric distance, respectively. Again, in the figure, the red curves denote the theoretical results, and the scatter red, green and blue plus symbols denote the R, T, and N observed values, respectively. The comparison between the
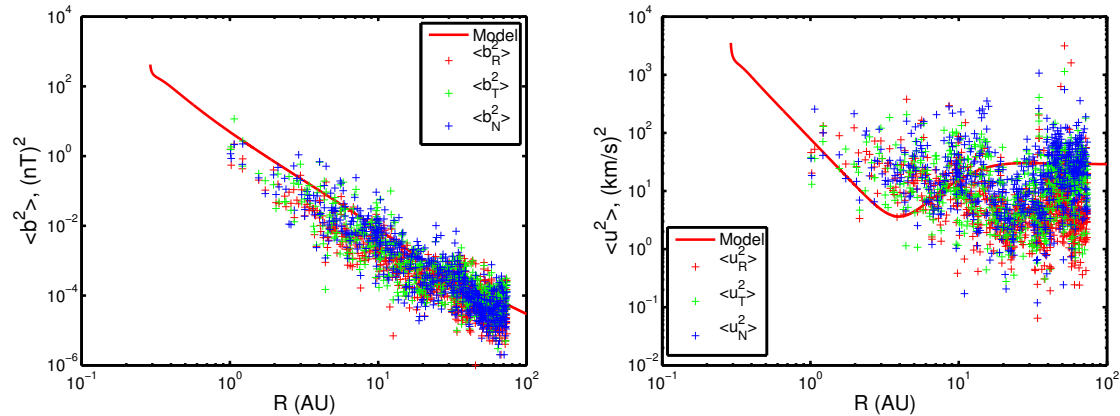
Figure A2. Left: Comparison of the fluctuating magnetic energy between the theoretical model and observations from 0.29 to 100 AU. Right: Comparison of the fluctuating kinetic energy from 0.29 to 100 AU. The scatter plus symbols denotes the observed values derived from *Voyager 2* 1-hr data. The suffix R, T, and N indicates the R-component, T-component, and N-component of the observed magnetic and kinetic energy.

theoretical and observed variance in the fluctuating magnetic field shows that both results are in a good agreement. In the case of the variance in the fluctuating solar wind speed, Figure 18 (right), the observed values within $\sim 5-6$ AU are closer to the theoretical results in comparison to the total observed fluctuating kinetic energy, Figure 14 (right).

Appendix B. Comparison to the R, T, and N component turbulent quantities related to the azimuthal angle

In this case, the R, T, and N component observed values are calculated considering the azimuthal angle ϕ. Note that the turbulent quantities are calculated for $0° < \phi < 180°$ and $180° < \phi < 360°$ separately, and then the results are combined. Figure 19 illustrates the total turbulent energy, the energy in forward propagating modes, the fluctuating magnetic energy density, and the energy in backward modes as a function of heliocentric distance in a clockwise direction, respectively. It is interesting to note that the trend of these observed values is similar to that of the previous observed values, where the sign of B_r was used to calculate the turbulent quantities. The theoretical and observed results also show similar trends from 1 to 75 AU.

The left and right panels of Figure 20 illustrate the variance in the magnetic field and the fluctuating kinetic energy with increasing the heliocentric distance, respectively. Again, these observed results are similar to that of the previous results, left and right panels of Figure 18.

Appendix C. Comparison to the R, T, and N component turbulent quantities related to a positive and negative sign of B_t

We also calculate the R, T, and N component turbulent quantities considering the sign of B_t. The comparison between the theoretical results and the R, T, and N component turbulent quantities with increasing heliocentric distance is shown in Figure 21, where the top left plot describes the total turbulent energy, the top right plot the energy in forward propagating modes, the bottom left plot the energy in backward propagating modes, and the bottom right plot the fluctuating magnetic energy density. It is observed that these turbulent quantities and the previous observed results, Figure 17 are the same. The left and right panel of Figure 22 illustrate
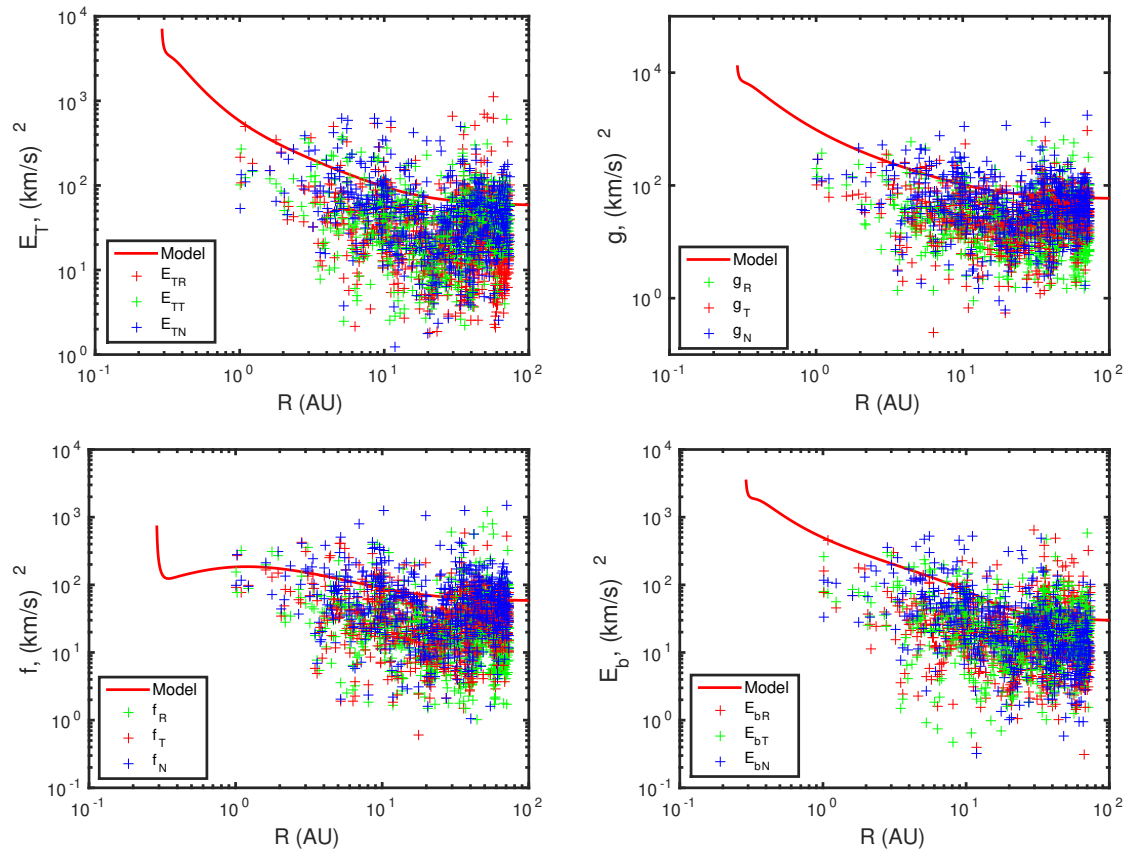
Figure B1. From top left in clockwise order, the plots show respectively the comparison of the theoretical model and the observed total turbulent energy, the energy in forward propagating modes, the fluctuating magnetic energy density, and the energy in backward propagating modes from 0.29 to 100 AU, respectively. The solid curves are theoretical results and the scatter plus symbols are observed values. The suffix R, T, and N indicates the R-component, T-component, and N-component of the observed values.

the variance in the fluctuating magnetic field and the fluctuating kinetic energy as a function of heliocentric distance, respectively.
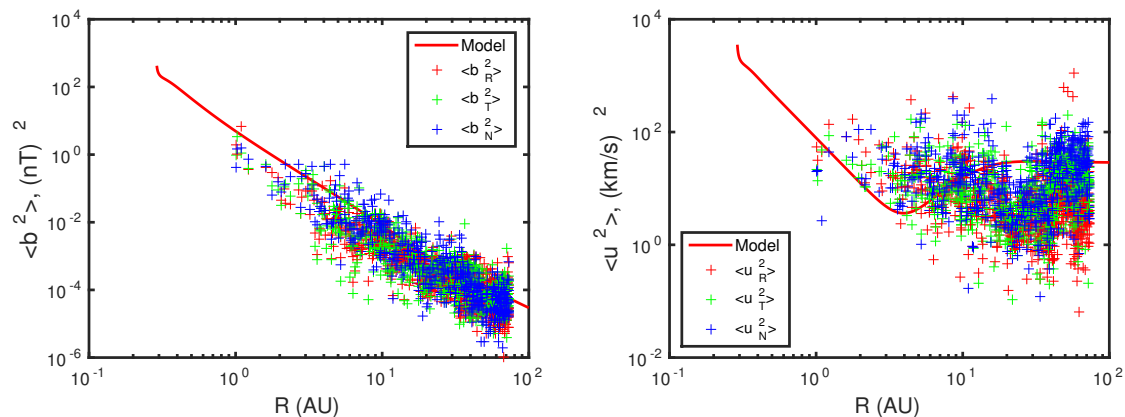
Figure B2. Left: Comparison of the fluctuating magnetic energy between the theoretical model and observations from 0.29 to 100 AU. Right: Comparison of the fluctuating kinetic energy from 0.29 to 100 AU. The scatter plus symbols denotes the observed values derived from *Voyager 2* 1-hr data. The suffix R, T, and N indicates the R-component, T-component, and N-component of the observed magnetic and kinetic energy.

References

[1] Bavassano B, Dobrowolny M, Mariani F, & Ness N F 1982 *J. Geophys. Res.* **87** 3617-3622
[2] Bruno R, & Carbone V 2005 *Living Reviews in Solar Physics* **2** 4
[3] Bruno R, & Carbone V 2013 *Living Reviews in Solar Physics* **10** 2
[4] Belcher J W, & Davis Jr L 1971 *J. Geophys. Res.* **76** 3534
[5] Coleman Jr P J 1968 *ApJ* **153** 371
[6] Goldstein M L, Roberts D A, & Matthaeus W H 1995 *ARA&A* **33** 283-326
[7] Tu C Y, & Marsch E 1995 *Space Sci. Rev.* **73** 1-210.
[8] Zhou Y, Matthaeus W H, & Dmitruk P 2004 *Reviews of Modern Physics* **76** 1015-1035
[9] Kraichnan R H 1965 *Physics of Fluids* **8** 1385-1387
[10] Belcher J W, Davis Jr L, and Smith E J 1969 *J. Geophys. Res.* **74** 2302
[11] Adhikari L, Zank G P, Hu Q, and Dosch A 2014 *ApJ* **793** 52
[12] Breech B, Matthaeus W H, Minnie J, Bieber J W, Oughton S, Smith C W, and Isenberg P A 2008 *Journal of Geophysical Research (Space Physics) 113* 8105
[13] Freeman J W 1988 *Geophys. Res. Lett.* **15** 88-91
[14] Gazis P R 1984 *J. Geophys. Res.* **89** 775-785
[15] Isenberg P A, Smith C W, and Matthaeus W H 2003 *ApJ* **592** 564-573
[16] Isenberg P A 2005 *ApJ* **623** 502-510
[17] Matthaeus W H, Zank G P, Smith C W, and Oughton S 1999b *Physical Review Letters* **82** 3444-3447
[18] Smith C W, Matthaeus W H, Zank G P, Ness N F, Oughton S, and Richardson J D 2001 *J. Geophys. Res.* **106** 825-8272
[19] Smith C W, Isenberg P A, Matthaeus W H, and Richardson J D 2006 *ApJ* **638** 508-517
[20] Smith C W, Vasquez B J, and Hamilton K 2006 *Journal of Geophysical Research (Space Physics)* **111** 9111
[21] Grappin R, Leorat J, and Pouquet A 1983 *A&A* **126** 51-58
[22] Müller W C and Grappin R 2005 *Physical Review Letters* **95** 114502
[23] Chen C H K, Bale S D, Salem C S and Maruca B A 2013 *ApJ* **770** 125
[24] Matthaeus W H, Oughton S, Pontius Jr, D H and Zhou Y 1994 *J. Geophys. Res.* **99** 19267
[25] Adhikari L, Zank G P, Bruno R, Telloni D, Hunana P, Dosch A, Marino R and Hu Q 2015 *The Astrophysical Journal* **805** 63
[26] Hollweg J V 1973 *ApJ* **181** 547-566
[27] Hollweg J V 1973 *J. Geophys. Res.* **78** 3643
[28] Hollweg J V 1974 *J. Geophys. Res.* **79** 1539
[29] Marsch E and Mangeney A 1987 *J. Geophys. Res.* **92** 7363-7367
[30] Marsch E and Tu C Y 1989 *Journal of Plasma Physics* **41** 479-491
[31] Marsch E and Tu C Y 1990 *J. Geophys. Res.* **95** 8211-8229
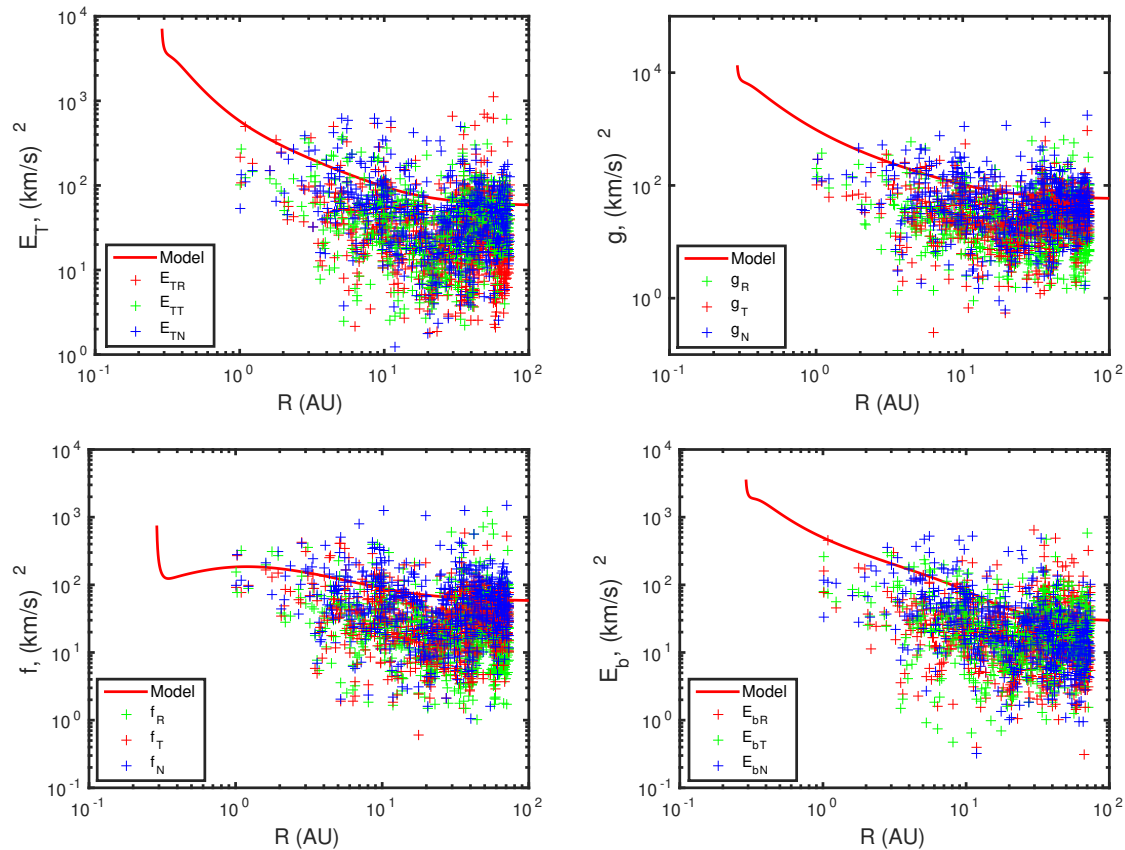
Figure C1. From top left in clockwise order, the plots show respectively the comparison of the theoretical model and the observed total turbulent energy, the energy in forward propagating modes, the fluctuating magnetic energy density, and the energy in backward propagating modes from 0.29 to 100 AU, respectively. The solid curves are theoretical results and the scatter plus symbols are observed values. The suffix R, T, and N indicates the R-component, T-component, and N-component of the observed values.

[32] Marsch E and Tu C Y 1990 *J. Geophys. Res.* **95** 11945-11956
[33] Elsässer W M 1950 *Phys. Rev.* **79** 183-183
[34] Zank G P, Matthaeus W H and Smith C W 1996 *J. Geophys. Res.* **101** 17093-17108
[35] Matthaeus W H, Minnie J, Breech B, Parhi S, Bieber J W and Oughton S 2004 *Geophys. Res. Lett.* **31** 12803
[36] Breech B, Matthaeus W H, Minnie J, Oughton S, Parhi S, Bieber J W, and Bavassano B 2005 *Geophys. Res. Lett.* **32** 6103
[37] Breech B, Matthaeus W H, Minnie J, Bieber J W, Oughton S, Smith C W, and Isenberg P A 2008 *Journal of Geophysical Research (Space Physics)* **113** 8105
[38] Zank G P, Dosch A, Hunana P, Florinski V, Matthaeus W H, and Webb G M 2012 *ApJ* **745** 35
[39] Whang Y C 1991 *Space Sci. Rev.* **57** 339-388
[40] Williams L L and Zank G P 1994 *J. Geophys. Res.* **99** 19229
[41] Burlaga L F and Ness N F 1994 *J. Geophys. Res.* **99** 19341
[42] Burlaga L F and Ness N F 1996 *J. Geophys. Res.* **101** 13473-13482
[43] Burlaga L F, Ness N F and McDonald F B 1995 *J. Geophys. Res.* **100** 14763-14772
[44] Matthaeus W H, Dasso S, Weygand J M, Milano L J, Smith C W, and Kivelson M G 2005 *Physical Review Letters* **95** 231101
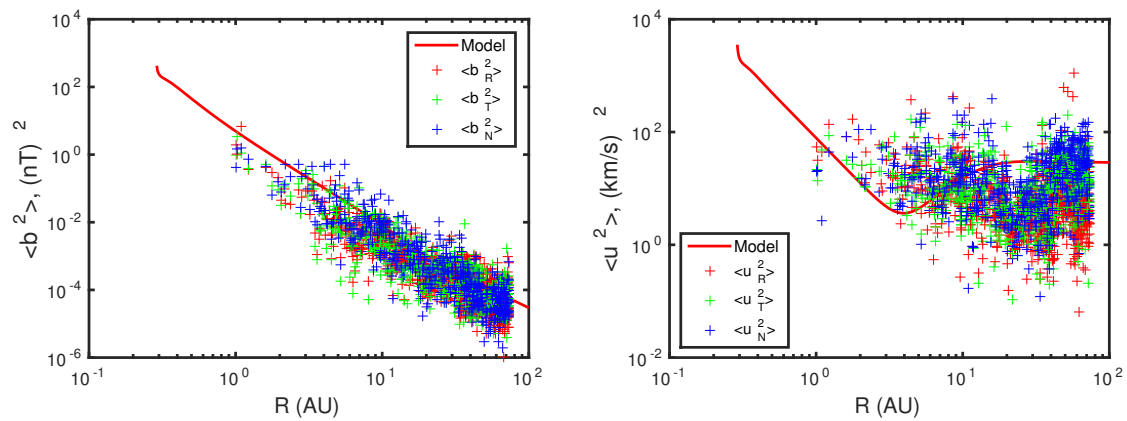
Figure C2. Left: Comparison of the fluctuating magnetic energy between the theoretical model and observations from 0.29 to 100 AU. Right: Comparison of the fluctuating kinetic energy from 0.29 to 100 AU. The scatter plus symbols denotes the observed values derived from *Voyager 2* 1-hr data. The suffix R, T, and N indicates the R-component, T-component, and N-component of the observed magnetic and kinetic energy.